

5.0 CATHODE FABRICATION FOR Co_3O_4 SPINEL

The focus of this project was to place cobalt oxide (Co_3O_4) spinel (COS) onto the surface of an electrode and demonstrate its ability to catalyze the water oxidation reaction. This lab has used a Nafion membrane covered conductive ITO glass electrode into which Mn-oxo cubane could be doped.⁴⁵ However, this is a poorly understood system which is limited by the diffusion of the cubane through the nafion membrane. Tilley et al. have shown that highly porous materials, such as nickel foam, can be used to chemisorb the spinel and create a uniform three dimensional electrode.⁴⁶ Extensions of Tilley's method as well as an exploration into conductive paints will be detailed here. The utility of all these methods was examined under both neutral and alkaline testing conditions. An electrode that was durable and easy to make with an eye towards a scalable industrial application was the goal.

5.1 EXPERIMENTAL

Spinel Synthesis: Two different synthesis methods were compared initially to find the best method for producing uniform COS nanoparticles. The first was a low temperature, solution-based synthesis introduced by Feng and Zeng (precipitation synthesis).⁴⁷ The second was a hydrothermal reaction detailed by Dong et al modified for a 23ml Parr acid digestion bomb (bomb synthesis).⁴⁸ After synthesizing, the particles were cleaned and separated via centrifuge as described in the literature. Finally the particles were dried in an oven at 100°C overnight. Both methods were characterized by powder XRD (Philips XPert powder diffractometer with sample changer) and by TEM (Topcon 002B).

Nickel Foam Preparation: Nickel foam was obtained from Marketech International and cut into 0.9cm x 0.9cm pieces with 2.0 mm thickness. These pieces were individually placed at the bottom of a quartz cuvette. One mL of a 1 mg/ml suspension of COS in iso-propanol was then added to the cuvette. After sonicating the cuvette for ten minutes, it was placed in an oven at 90°C until completely dried. Using gravimetric analysis, the foam was found to have an average loading of about 0.4 mg/cm² (area measured as simple face geometric area).

Conductive Paint Preparation: Silver and carbon conductive paints were obtained from SPI Supplies. A 1:1 ethanol:paint dilution was made of the silver paint, and a 3:1 i-propanol:paint dilution was made of the carbon paint. These dilutions were then mixed via sonication with spinel nanoparticles to get an even dispersion. A Crescendo 175 airbrush (using house nitrogen as the air source) was used to apply the paint in a uniform coating onto conductive ITO glass. The sample was dried at 75°C for 30 minutes before use. Loading of the spinel on the plate was determined by gravimetric analysis and measurement of the surface area of the ITO being covered by paint.

Electrochemical Analysis: All samples were analyzed via linear sweep cyclic voltammetry (CV) (Princeton Applied Research PARstat 2263) and constant voltage bulk electrolysis (HCH Instruments Electrochemical Workstation). A three neck cell was used to hold a platinum mesh counter electrode, Ag/AgCl reference electrode, and the working electrode for both types of measurements. 1M KOH (pH 13) and 0.1 M Na₂SO₄ (pH 6.5) were used for electrolytes during testing. A scan rate of 50mV/sec was used during the CV sweeps unless otherwise noted. (Note: 1M KOH was found to be pH 13 due to the initial addition of naturally acidic distilled water when making solution.)

5.2 RESULTS/DISCUSSION

Synthetic Procedure Comparison: P-XRD was used to confirm that both syntheses successfully made COS (See Supplemental Fig 9.2.1). The peaks obtained matched well with database information about cobalt oxide spinel and there was also a distinct absence of the characteristic peaks of CoO_2 and Co(OH) , which are the bulk phase and a possible impurity in the nanoparticle spinel. TEM showed that both syntheses produced particles less than 20 nanometers in size that were fairly uniform (Fig. 14 A & B).

However, the precipitation synthesis did produce some much larger particles ($\sim 50\text{nm}$) (Fig 14 C inset). Uniformity of catalyst size is highly desirable to maintain a high surface area to volume ratio. The bomb synthesis particles were more cubic in shape than the precipitation

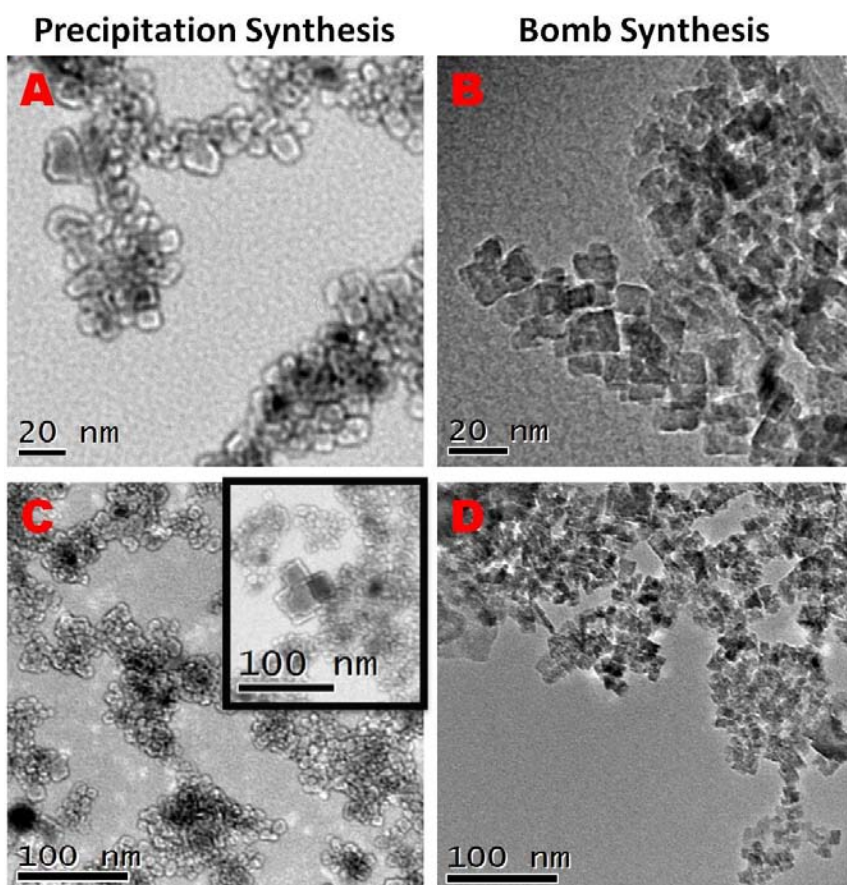


Figure 14. TEM images of COS from different synthesis methods

particles (Fig 14 C & D). The bomb synthesis also produced similar amount of product with 20 times less starting material. Finally the bomb synthesis mimics more closely a true industrial method that could be scaled to bigger pressurized reactors. Thus, the nanoparticles from the bomb synthesis method were chosen to be used throughout the tests conducted here.

Nickel Foam Electrode: Nickel foam with COS deposited was shown to be active for water oxidation in both alkaline and neutral pHs. In pH 13 solution (1M KOH) the oxidation potential for water vs. Ag/AgCl is 0.25 V, and in pH 6.5 (0.1M Na₂SO₄) it is 0.64 V. Both potentials were calculated using the Nernst equation:

$$E = E^0 - \frac{0.05916 V}{z} \log_{10} \left(\frac{a_{Red}}{a_{Ox}} \right) \quad \text{Eq. 4}$$

Under alkaline conditions, the bare nickel foam was also found to be reactive, while it remained inactive under neutral conditions. The bare foam showed an oxidation peak at ~0.4V (vs. Ag/AgCl) under alkaline conditions with a catalytic current starting ~0.5 V (vs. Ag/AgCl) (Fig. 15). In neutral pH the nickel foam showed no reactivity with only a small catalytic current forming ~1.0 V (vs. Ag/AgCl).

At alkaline pH, the loaded nickel foam displayed first an anodic oxidation peak at ~475 mV, which can be attributed to the reaction of the spinel with the excess hydroxide in solution (Rxn. 6). As Tilley described, in alkaline pH a likely catalytic reaction process is Rxns 6 – 8, where S represents the catalytic site.⁴⁹



Then, as catalytic turnovers occur, a dramatically increasing current can be observed starting around 550 mV. These two factors are indicative of spinel attachment to the nickel foam and are similar to the results Tilley observed.

At pH 7 the reaction scheme above no longer applies. Thus there is no longer an initial peak due to SOH; however, there is still a clear catalytic current that begins to develop ~825mV

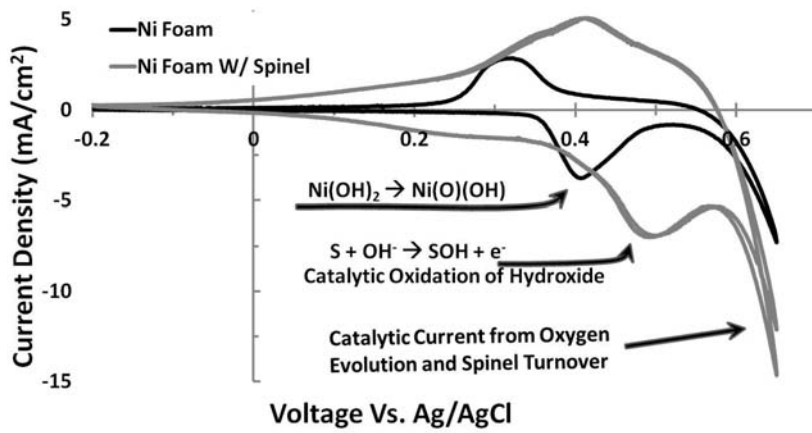


Figure 15. Plot of the current density versus voltage for nickel foam both with and without spinel deposited on the surface at pH 13. The key features of the scans have been identified on the plot.

the nickel foam is the shifting oxidation peak. In the nickel foam background CV, a strong peak can be observed at $\sim 400\text{mV}$, while the oxidation peak shifts to $\sim 475\text{mV}$ for the foam loaded with spinel. The peak at $\sim 400\text{mV}$ is attributed to the reaction of the bare nickel foam with hydroxide in solution. The absence of this peak in the loaded sample suggests complete coverage of the nickel surface, thus preventing this reaction. This hypothesis is supported by the series of graphs in Fig. 17, where samples of nickel foam were treated with the same amount of spinel but different outcomes resulted. Inset B indicates that when incomplete coverage occurs, both the oxidation peaks at $\sim 400\text{mV}$ and $\sim 475\text{mV}$ can be seen. However, under proposed total coverage conditions (inset C) only the oxidation peak at $\sim 475\text{mV}$ can be observed. Inset D in Fig. 17 shows the progression from poor to complete coverage.

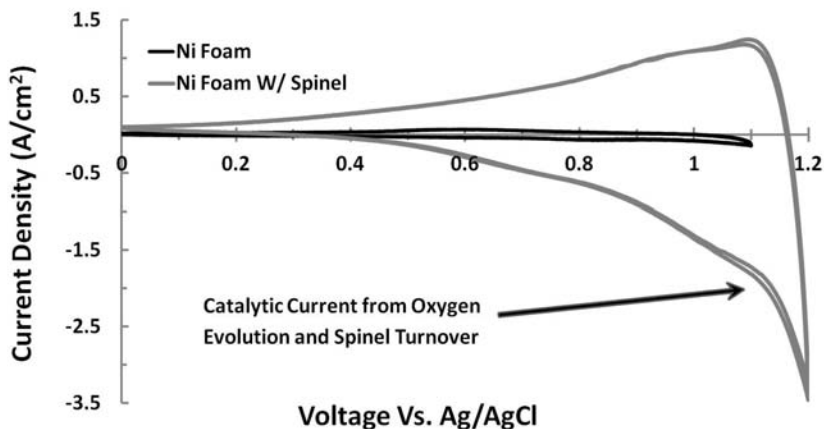


Figure 16. Plot of the current density versus voltage for nickel foam both with and without spinel deposited on the surface at pH 6.5.

(Fig. 16). The large increase in current over the baseline indicates the presence and continued activity of the COS despite the change in pH.

An important note on the cyclic voltammetry scans run in alkaline conditions for

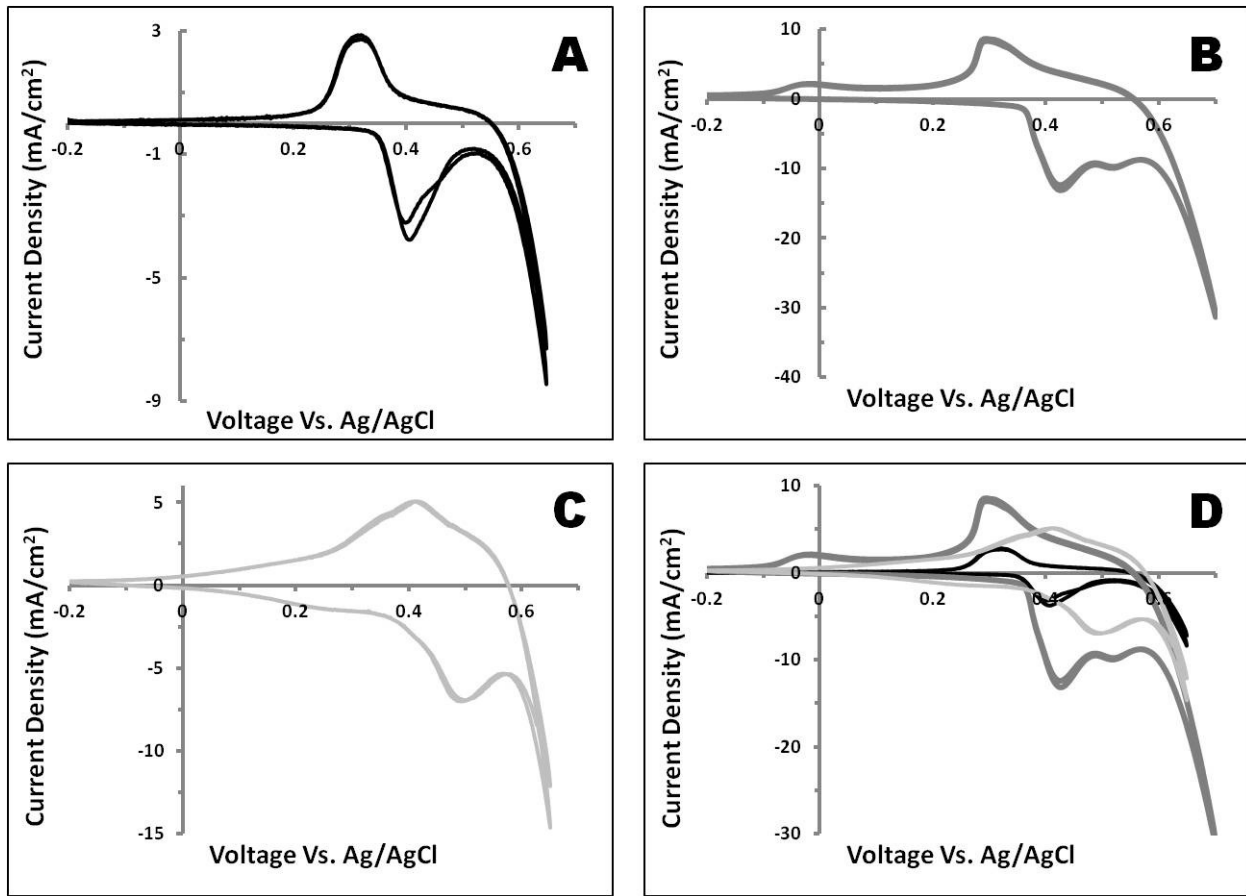


Figure 17. Progression of current density vs. voltage plots that show change from bare nickel foam (A) to nickel foam poorly covered by the COS (B) to nickel foam completely covered by the COS (C). D shows the three plots overlayed onto each other. All scans were taken at 50mV/sec and at pH 13.

Conductive Paint (Carbon): Conductive paints were explored because of the easy means by which they can be applied to a surface and their general good adherence. They are also readily available through many manufacturers. Two conductive paints from SPI Supplies were used as vehicles for spinel dispersions: silver paint and carbon paint. The silver paint was found not to be useful however because it underwent electrochemical reaction within the region of interest for water oxidation. This created a very strong background current which was not desirable when examining the activity of water oxidation catalysts. Carbon paint was tested next because it was less-reactive and also represented a much cheaper alternative than platinum paint.

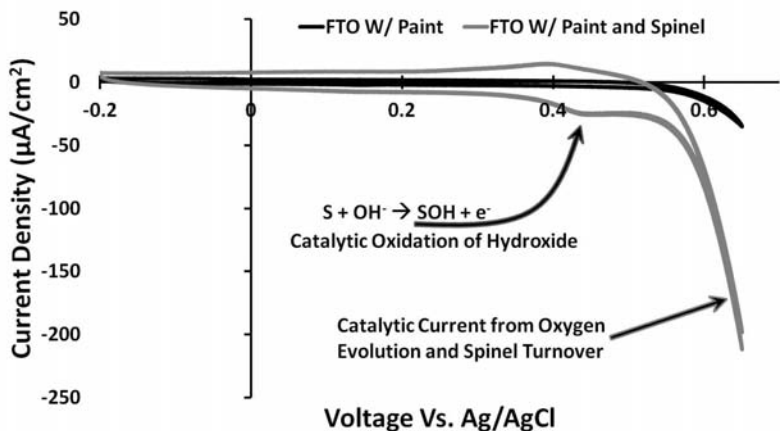


Figure 18. Plot of the current versus voltage for carbon paint both pure and doped with COS on conductive glass plates at pH 13. The key features of the scans have been identified on the plot.

Carbon paint was found to successfully adhere the COS to the surface of the electrode. In 1M KOH a similar oxidation peak can be seen at ~425mV and catalytic current forms at ~500mV (Fig. 18). It also showed a catalytic current in 0.1M Na₂SO₄ (Fig. 19).

While the carbon paint was successful in attaching the spinel to the ITO surface, the amount of current produced by this electrode was substantially less than that produced by the doped nickel foam (Fig. 20). However, this is to be expected because the nickel foam is a three dimensional electrode and therefore provides a much larger surface area for chemical interaction. The foam is also extremely porous allowing for much higher loadings of the spinel. Due to the fact that these two electrodes are of different dimensionality, it is meaningless to compare the CVs. A more realistic comparison of the two electrodes is turn over frequency (TOF).

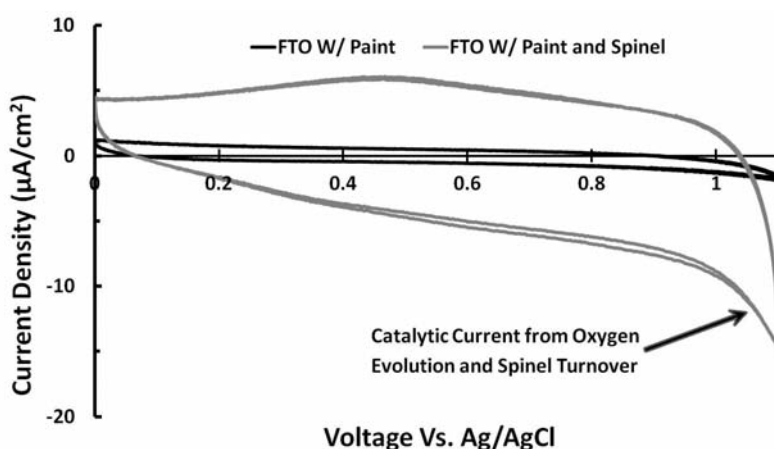


Figure 19. Plot of the current versus voltage for carbon paint both pure and doped with COS on conductive glass plates at pH 6.5. The key features of the scans have been identified on the plot.

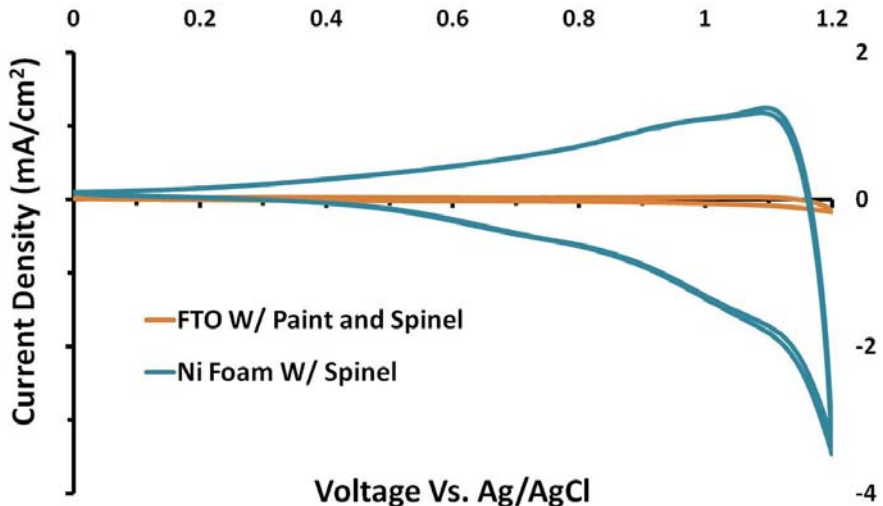


Figure 20. Comparison of the IV scans for the nickel foam covered with spinel and the carbon paint doped with spinel. This plot compares the data obtained at pH 6.5.

Turn Over Frequency: TOF was calculated from bulk electrolysis data taken at different voltages for both nickel foam and carbon paint samples in 1M KOH and 0.1M Na₂SO₄. The number was calculated by taking the approximate steady-state current density from the bulk electrolysis and converting that in the following manner.

$$\frac{\text{Amps}}{\text{sec} * \text{cm}^2} * \frac{6.24 * 10^{18} \text{ electrons}}{\text{Amp}} * \frac{1 \text{ O}_2 \text{ molecule evolved}}{4 \text{ electrons}} * \frac{1 \text{ mol O}_2 \text{ evolved}}{6.02 * 10^{23}} \quad \text{Eq. 5}$$

$$* \frac{1}{\text{molar density spinel}} * \frac{1 \text{ mol spinel}}{3 \text{ mol Cobalt}} = \frac{\text{mols O}_2 \text{ produced}}{\text{mol Co} * \text{sec}} = \text{TOF}$$

The TOF and their number of replicates are summarized in Table 2 and Table 3 for 0.1M Na₂SO₄ and 1 M KOH respectively.

Table 2. TOF for two electrodes in 0.1 M Na₂SO₄

Over Potential	0.1M Na ₂ SO ₄ TOF + %STD (Number of Replicates)	
	Carbon Paint	Nickel Foam
260 mV	6.8 E-06 ± 37% (3)	1.4 E-05 ± 26% (2)
360 mV	1.1 E-05 ± 72% (4)	1.8 E-05 ± 49% (2)
410 mV	2.2 E-05 ± 49% (4)	2.3 E-05 ± 46% (2)
460 mV	4.3 E-05 ± 33% (4)	3.9 E-05 ± 44% (2)
510 mV	9.6 E-05 ± 23% (4)	8.6 E-05 ± 35% (2)

Table 3. TOF for two electrodes in 1M KOH

Over Potential	1 M KOH TOF + %STD (Number of Replicates)	
	Carbon Paint	Nickel Foam
240 mV	~	1.9 E-04 ± 94% (2)
290 mV	~	7.6 E-04 ± 18% (2)
340 mV	3.0 E-3 (1)	5.0 E-03 ± 9% (2)
390 mV	~	2.8 E-02 ± 24% (2)

The TOF in the tables above give a much better idea as to whether or not these two systems provide a comparable level of electronic connection between the COS and the electrode. In Table 2 it can be seen that the carbon paint and nickel foam TOFs trade for the higher number, but in most cases they are within the experimental error of each other. In Table 3 there is not much comparison because time constraints prevented complete carbon paint data from being taken; however, for the one overpotential the two systems provided similar TOF. This work is planned to be completed in the future. The upperbounded 390 mV overpotential in 1M KOH for nickel foam also produced a TOF similar to that found by Tilley at an overpotential of 388mV (9.3 E -2).⁵⁰ However, it should be noted that his system was reported to be at pH 14, thus decreasing the potential at which water oxidation occurs as compared to the system used here which was at pH 13.

It is also important to note that the 1M KOH samples were able to achieve TOF similar to that obtained out of the Clark electrode Ru(II) bipyradine assay (4.25×10^{-3} mmol O₂ / mmol Co / min). This was the in-solution method by which the activity of catalysts was previously determined in this lab, which was limited by the fact that it required a terminal electron acceptor (persulfate) and expensive dye (Ru(II)). The importance of the comparison is that this was a photoactive system in which the variables affecting the TOF were not easily controlled. The carbon paint system probes exclusively the activity of the catalysts without any other reaction and electron transfer limitations that exist in the Clark electrode assay. Thus in order for the carbon paint or nickel foam electrode to be considered a success, it must be able to produce TOF better or of the same order of magnitude as the Clark electrode assay.

There is one key difference in how the nickel foam and carbon paint data was handled. In both cases background bulk electrolysis data was taken for normalization purposes; however, this normalization was not done for the nickel foam data in 1M KOH. Upon examination of the overlain background and doped scans, it was clear that for some scans at low overpotentials, the background current was actually higher than that of the nickel foam with spinel. However, at higher overpotentials the doped nickel far outstripped the bare nickel foam (Fig. 21). This has been attributed to the nickel oxidation reaction which occurs at a lower potential than the nickel oxidation of water (Fig. 15). The current measured in the backgrounds on this bare nickel is not due to water oxidation but rather to the hydroxide reaction. However, this current would not contribute to the measurements taken of the doped nickel foam if the nickel was completely covered, as proposed above. Thus the background current for nickel foam was not normalized out when calculating TOF.

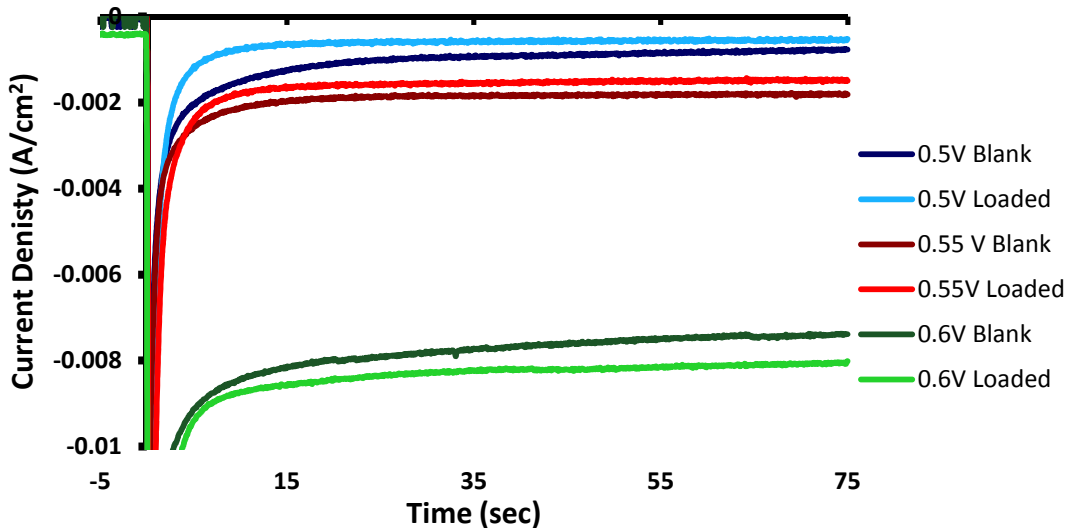


Figure 21. Plot of current density decay over time at given voltages for both bare nickel foam (blank) and nickel foam loaded with spinel nanoparticles (loaded).

Note on Stability: The carbon paint was sturdy and could withstand extended CV scans without decay. It was also resistant to light pressure and could be handled easily with gloves. The carbon paint did exhibit some stability problems in alkaline solution. In the 1M KOH experiments, it was not uncommon for the thin film of paint to delaminate from the surface of the ITO. The film would last throughout the testing, but as it was removed from solution the film would come off or be washed off when rinsed with water. It is unclear at this time whether the delaminating is the product of the alkaline conditions or the product of bubble evolution within the thin film. There were no stability issues at neutral pH.

A procedure was developed to keep these films intact and was successfully tested. After testing in alkaline conditions, the film needed to be carefully removed, then allowed to air-dry overnight at least. Once dry, it was carefully dipped into a beaker of d-H₂O and allowed to sit for 5 minutes. Carefully remove the sample from the water and then place it in the oven at 75°C until dry. At this point the film appeared to have strongly reattached to the ITO and could be handled freely and rinsed at will.

5.3 CONCLUSION/FUTURE WORK

Several different methods of placing cobalt oxide spinel onto an electrode were explored. Nickel foam, which had previously been utilized by Tilley, was explored further in comparison to two new products: silver and carbon paint. The carbon paint was found to successfully create electrical contact between the spinel catalyst and the conductive ITO electrode; however, the silver paint was electrochemically active in the area of interest.

The nickel foam loaded electrodes were shown to produce similar data to that demonstrated by Tilley in 1M KOH. The utility of this electrode was also extended to neutral pH where it again was shown capable of catalytic activity. Carbon paint electrodes demonstrated similar trends to those of the nickel foam data, thus indicating that the spinel catalyst was successfully paired in this system as well. The carbon paint electrodes were not capable of producing as much current as the nickel foam but this is attributed to the lack of a three dimensional framework in the carbon paint. While it is not a three dimensional electrode, the carbon paint electrode was able to produce comparable TOFs.

It would be beneficial to this research if additional duplicate carbon paint electrode data could be obtained, especially to obtain TOF in 1 M KOH. The effects of different loadings of catalyst in the original paint should be explored as it could prove to greatly increase the activity of these slides. It is also necessary to obtain gas chromatography-mass spec data on the gases evolved from these cells to make certain only hydrogen and oxygen are being produced.

This work was conducted at Rutgers University with the assistance of David Robison and under the supervision of Dr. Charles Dismukes and Prof. Tewodros Asefa.

6.0 EFFECTS OF PLD OF SrTiO₃ ONTO TiO₂ NANOTUBES

In this project it was desired to see if a more beneficial interaction between TiO₂ nanotubes and SrTiO₃ could be produced if a pulse laser deposition method was used instead of the previously used hydrothermal method. PLD eliminates the major problem with the hydrothermal method because it does not affect the TiO₂ nanotube structure. PLD only lays a thin film of SrTiO₃ on top of the surface. It was also postulated that some of the SrTiO₃ would penetrate into the nanotubes, resulting in a good amount of surface contact between the materials. This is one of the reasons nanotubes were expected to perform better here than nanoparticles would. It was found that for an optimal thickness of SrTiO₃ deposited, the photocurrent and photovoltage of the cell increased.

6.1 EXPERIMENTAL

Materials and Preparation: Ti metal (0.25 mm, 99.5% purity) was purchased from Alfa Aesar. 4 cm by 0.8 cm strips were cut and sonicated in 2-propanol for one hour, before being stored in acetone until use. Ammonium fluoride (Sigma Aldrich), Potassium hydroxide pellets (Fisher Scientific), and P-25 (Degussa) were purchased and used as received.

Ordered TiO₂ nanotubes were prepared via a standard electrochemical etching process from the Ti foil.⁵¹ Clean Ti foil was dried and suspended in a three arm cell. The electrolyte used was 98% by volume ethylene glycol, 2% by volume water, and 0.27M ammonium fluoride. The counter electrode was platinum mesh. The Ti film was connected to the positive lead of a voltammeter and the platinum electrode was connected to the negative lead. The voltage was ramped up at ~1V/sec to 60V where it was left for one hour. After one hour, with the power

supply still on, the Ti foil was removed and dropped into distilled water and sonicated for ~2-3 seconds to remove surface contaminates. The foils were quickly air dried and then annealed in the following way: 2°C/min ramp up to 450°C, hold for 3 hours, 2°C/min ramp down to 25°C. This process yields nanotubes with lengths of 5 to 10 μm and diameters of approximately 50 nm.

TiO₂ nanoparticle films were prepared by first sonicating 3.5g of P25 powder in 15 mL of ethanol and adding a few drops of titanium isopropoxide to form a paste. The as-prepared paste was then doctor-bladed onto a fluorine-doped tin oxide (FTO) substrate that had been cleaned with acetone and ethanol. The film was allowed to dry at room temperature and was then annealed at 400°C for 1 hour. The resulting films were approximately 10 μm thick.

SrTiO₃ thin films were deposited onto the substrates using PLD with a KrF laser. The deposition conditions were 120 mJ laser power at a pulse rate of 20 Hz in a background atmosphere of 75 mTorr of oxygen. Under these conditions, the deposition rate was 31.4 nm SrTiO₃/min. The stage was held at room temperature and the length of deposition was used to control film thickness. The target was a SrTiO₃ disk prepared using commercial SrTiO₃ powder compressed and sintered at 5000 lbs and 800°C for 2 hours. After deposition an additional annealing step (450 °C for 3 hrs) was taken to increase the crystallinity of the SrTiO₃ thin film.

Characterization: Samples were analyzed via chronoamperometric, open circuit potential, and current-voltage (I-V) measurements made using a Princeton Applied Research PARstat 2273 potentiostat. A 3-electrode cell with platinum mesh as the counter electrode and Ag/AgCl (saturated KCl) as the reference electrode was used to take these measurements. All voltages, unless otherwise indicated, are measured against this Ag/AgCl reference. A 300W xenon lamp with an AM 1.5G filter (Newport) was used as the white light source. The sample was

positioned so that the incident power was 100 mW/cm^2 with an illumination area of 0.28 cm^2 . IPCE measurements were carried out in a two-electrode setup under no applied bias with a platinum mesh counter electrode using a Bausch and Lomb high-throughput monochromator with $\sim 10 \text{ nm FWHM}$ and a Keithley 617 programmable electrometer. The electrolyte used for both setups was 1M KOH. Scanning electron micrograph (SEM) images were taken on an FEI Magellan 400.

6.2 RESULTS/DISCUSSION

SEM Analysis of Film Morphology: SEM images of the TiO_2 nanotube array with increasing SrTiO_3 layer thickness were taken to analyze the morphology of the thin film growth. Ti foil was used as a base case to compare against the morphologies on the TiO_2 nanotubes against. It was found that the films acted similarly on both substrates. It is clear from Figure 22 that a

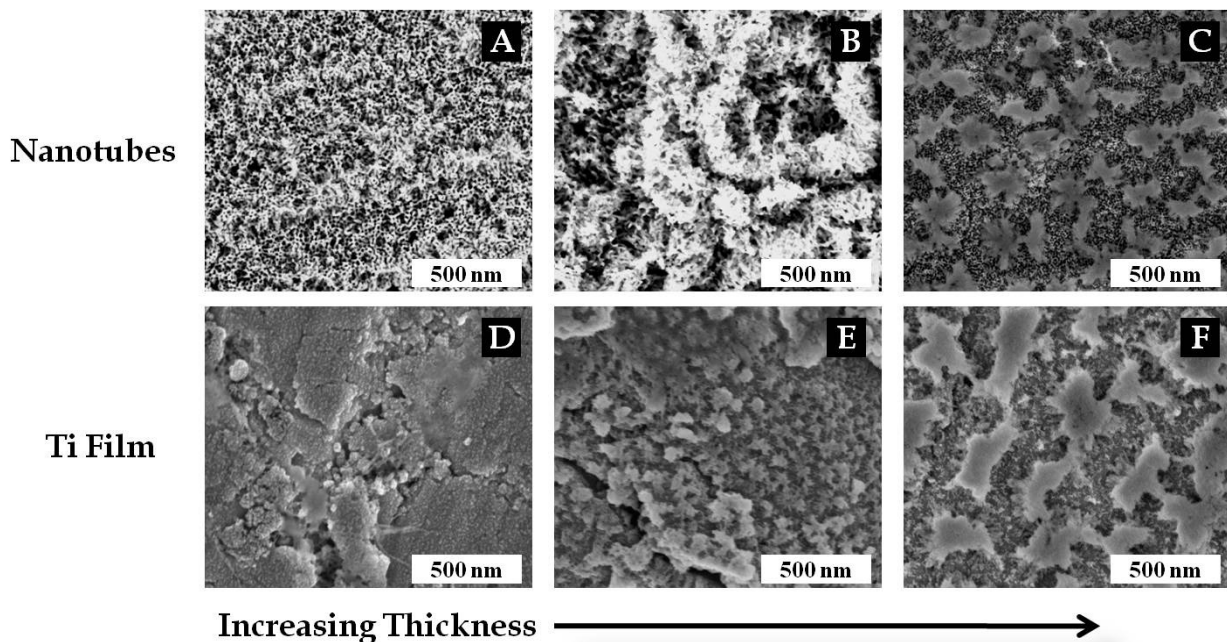
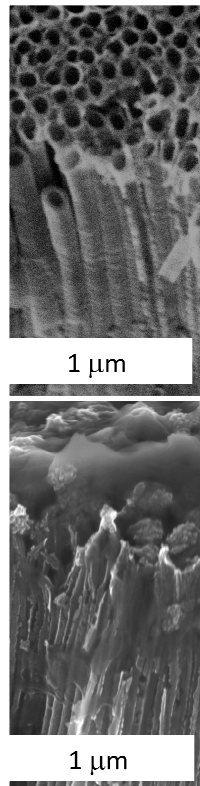


Figure 22. SEM pictures of SrTiO_3 deposited on TiO_2 nanotubes (A,B,C) and Ti foil (D,E,F) over increasing thickness of SrTiO_3 layer from 31 nm (A,D) to 155 nm (B,E) to 470 nm (C,F).

uniform layer of SrTiO₃ is not deposited. Even on the comparatively smooth surface of the Ti foil, aggregate clusters can be seen forming on the surface. As the thickness of the film increased, a more defined SrTiO₃ film can be seen, although there are still clusters growing in size on the surface. This indicates that there are preferential crystal growth positions on the substrate where the islands begin to form. Figure 23 shows a cross sectional view of the original TiO₂ nanotubes (A) and a view of the TiO₂ nanotubes with SrTiO₃ deposited (B). It is important to notice that there is some penetration of the SrTiO₃ film into the TiO₂ nanotube array, although it by no means penetrates the entire length of the tubes.

Effect of Post Deposition Annealing: Following the deposition of the SrTiO₃ onto the nanotubes substrate, the cell was again annealed for 3 hours at 450°C. This annealing step was found to be crucial because little or no improvements in measured photocurrent or photovoltage



es of cross-section
ays with (A) and
D₃ deposited

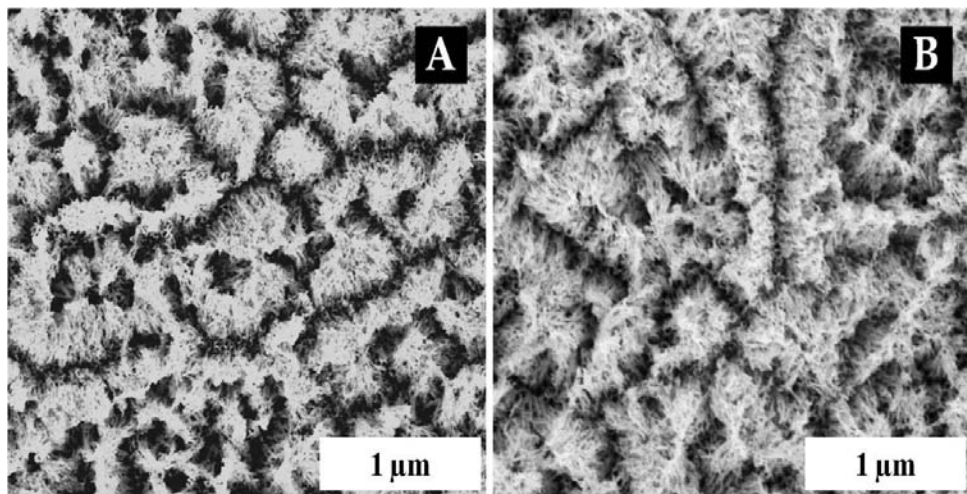


Figure 23.
SEM pictures of
157nm layer of
SrTiO₃ on TiO₂
nanotubes before (A)
and after annealing
(B). Note the fewer
number of hills
present in picture B
due to the continued
agglomeration

over the baseline cell occurred without it. This indicates that PLD does not create a good interface between the TiO_2 nanotube array and the SrTiO_3 nanoparticle layer. SEM images taken before and after annealing the SrTiO_3 layer also showed some continued agglomeration of the SrTiO_3 clusters indicating the layers reorganization during the annealing (Fig. 24). Presumably, annealing a second time would further improve the interface and increase further the photocurrent and photovoltage measured.

In addition it was found that the annealing of the SrTiO_3 layer needed to be performed before any IV measurements were taken. If measurements were taken before the annealing process and then after, the improvements previously ascribed to the annealing step did not occur. In other words, despite the annealing step, the cell showed the same activity as if the annealing step had not been taken. The reason for why taking measurements before annealing had this affect on subsequent trials is unclear, although it may be due to residual potassium ions from the 1 M KOH electrolyte used adsorbed onto the electrode surface hindering the recrystallization process of the SrTiO_3 . This occurred despite attempts to wash the samples after immersion in the electrolyte.

Improved Photo Response: Figure 25 shows the chronoamperometric response of TiO_2 nanotube arrays to illumination with increasing thicknesses of SrTiO_3 . A maximum is reached at a SrTiO_3 film thickness of 155 nm with a slightly lower plateau occurring at higher thicknesses. This

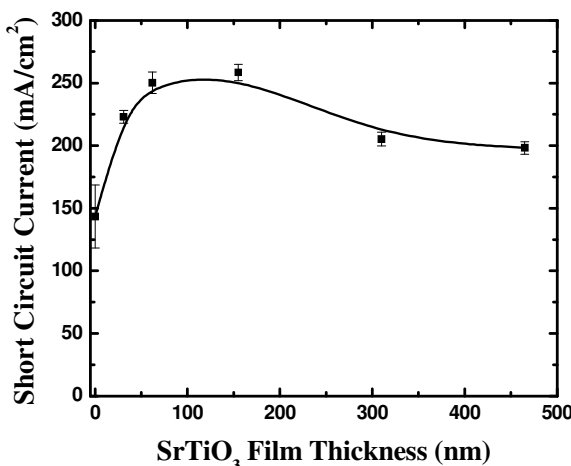


Figure 25. Photocurrent generated for different SrTiO_3 film thicknesses deposited on TiO_2 nanotube arrays.

represents an optimal thickness where efficient charge separation is achieved while recombination losses are minimized in the SrTiO₃ layer. In the context of water-splitting applications, this increase in photocurrent represents a greater possible rate of hydrogen production at the counter electrode of the circuit.

Figure 26 shows how the open circuit potential also increases with greater SrTiO₃ film

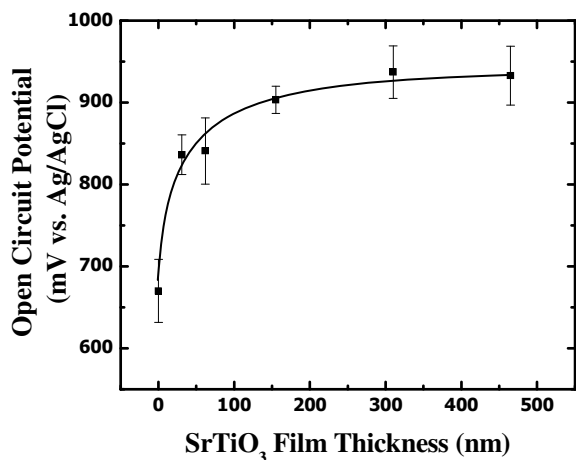


Figure 27. Open circuit potential measured at different SrTiO₃ film thicknesses on TiO₂ nanotube arrays.

Fermi level for the heterostructure material while under illumination. In water splitting applications, the higher energy electrons will provide a greater driving force to reduce hydrogen at the counter electrode.

Current-voltage (IV) curves confirm the trend observed in both the photocurrent and photovoltage measurements (Fig. 27). As the SrTiO₃ film thickness increases, both the open circuit potential and the short circuit current increases to a maximum at a SrTiO₃ film

thicknesses. The change in photovoltage generated increased to a plateau of approximately 900mV (300 mV above the baseline measurement), reached again at a SrTiO₃ film thickness of 155 nm. This increase in potential is attributed to the more negative conduction band of the SrTiO₃, resulting in a more negative overall

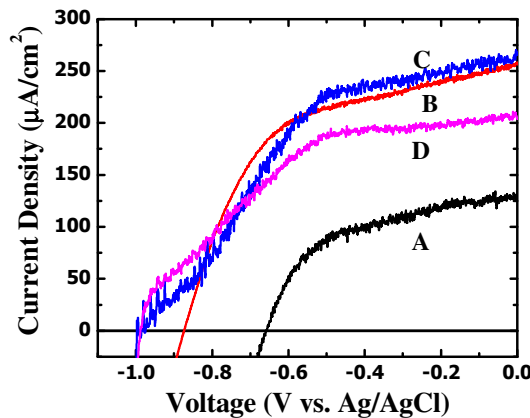


Figure 26. IV curves for TiO₂ nanotube arrays (A) without SrTiO₃ and with (B) 31 nm SrTiO₃, (C) 155 nm SrTiO₃, and (D) 470 nm SrTiO₃.

thickness of 155 nm.

The increase in photocurrent could be attributed to either a modification of the TiO₂ band gap or to decreased recombination in the SrTiO₃-TiO₂ nanotube array heterostructure due to increased charge separation. Incident Photon-to-Charge-Carrier Efficiency (IPCE) measurements were obtained by Ben Meekins and used to establish the onset of photocurrent activity. The IPCE values were calculated using Equation 6,

$$IPCE(\%) = \frac{1240 * I_{SC}}{\lambda * P_{INC}} \quad \text{Eq. 6}$$

where I_{SC} is the current measured and P_{INC} is the incident power at a particular wavelength of light. The incident light power is determined by a photodiode with calibrated responsivity.

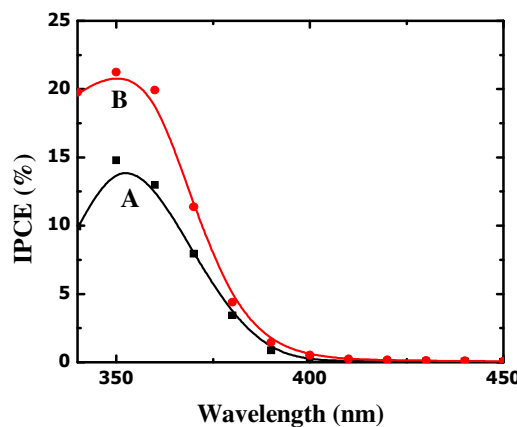


Figure 28. IPCE curves (a) before and (b) after 470 nm SrTiO₃ films deposited on TiO₂ nanotube arrays.

These measurements (Fig. 28) prove that the band gap of TiO₂ was unchanged by the SrTiO₃ deposition. If the band gap had been modified the onset of photocurrent would have been shifted to a lower energy wavelength of light. Since this was not observed, but rather increased efficiency at the same wavelength was, the increased photocurrent can be attributed to enhanced charge separation,

with holes moving to the SrTiO₃ nanoparticles to be scavenged by the electrolyte and electrons flowing to the TiO₂ nanotubes to travel through the external circuit.

Open circuit potential decay measurements support this explanation for the observed increase in photocurrent. Electron lifetimes after deposition of SrTiO₃ were longer at all

thicknesses, but the difference at 155 nm is the most significant. The electron lifetime was calculated using Equation 7,

$$\tau = \frac{k_B T}{e} \left(\frac{dV_{oc}}{dt} \right)^{-1} \quad \text{Eq. 7}$$

where k_B is the Boltzmann constant, e is the elemental charge, and τ is the electron lifetime.⁵²

Figure 29 is a representative plot that shows how the electron lifetime changes with respect to the open circuit potential. The lifetime is longer at more negative potentials for the SrTiO₃-TiO₂ nanotube array composite as compared to the TiO₂ nanotube array alone. Accordingly, the increased photocurrent generated is attributed to a decreased rate of recombination in the composite SrTiO₃-TiO₂ material caused by the physical separation of the electrons and holes

generated in the heterostructure.

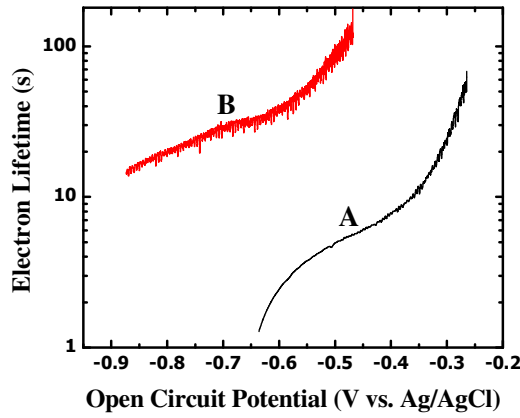


Figure 29. Electron lifetime versus open circuit potential as calculated for TiO₂ nanotube array electrodes (a) without SrTiO₃ and (b) with 155 nm layer of SrTiO₃

it may be due to increased recombination at the interface between the SrTiO₃ and TiO₂ nanoparticles.

The hypothesis that TiO₂ nanotubes would perform better than TiO₂ nanoparticles was also tested. The optimal thickness of SrTiO₃ was also deposited onto a nanoparticle thin film (created as described in the experimental section). The photocurrent and photovoltage measured were significantly worse than those of the TiO₂ nanotube cell. The reason for this is not clear, but

6.3 CONCLUSION/FUTURE WORK

Deposition of SrTiO₃ via PLD onto a TiO₂ nanotube substrate creates a beneficial charge separation interaction which allows for an increase in photocurrent and photovoltage. An optimum thickness of 155 nm of SrTiO₃ was found, which resulted in ~300mV increase in photovoltage and ~100 μ A/cm² increase in photocurrent over TiO₂ nanotubes alone. The increase in photovoltage is attributed to the more negative conduction band of SrTiO₃, which causes the Fermi level of the composite material to become more negative. The increase in photocurrent is attributed to decreased recombination in the composite material as compared to the TiO₂ nanotubes alone. Increased efficiency at the same wavelength in the IPCE measurements and increased electron lifetimes confirm these conclusions about the source of the improvements. The sequence of the post-deposition annealing process was also found to be a crucial part of the preparation. Finally it was found that SrTiO₃ did partially penetrate into the nanotubes array. More intimate contact between TiO₂ and SrTiO₃ should result in further improvements in the heterostructure's photovoltaic performance.

This work was conducted at the University of Notre Dame with the assistance of Ben Meekins and under the supervision of Prof. Prashant Kamat and Prof. Paul McGinn.